Effects of Urban Surfaces and White Roofs on Global and Regional Climate

MARK Z. JACOBSON AND JOHN E. TEN HOEVE

Department of Civil and Environmental Engineering, Stanford University, Stanford, California

(Manuscript received 14 January 2011, in final form 11 September 2011)

ABSTRACT

Land use, vegetation, albedo, and soil-type data are combined in a global model that accounts for roofs and roads at near their actual resolution to quantify the effects of urban surface and white roofs on climate. In 2005, ~0.128% of the earth's surface contained urban land cover, half of which was vegetated. Urban land cover was modeled over 20 years to increase gross global warming (warming before cooling due to aerosols and albedo change are accounted for) by 0.06–0.11 K and population-weighted warming by 0.16–0.31 K, based on two simulations under different conditions. As such, the urban heat island (UHI) effect may contribute to 2%–4% of gross global warming, although the uncertainty range is likely larger than the model range presented, and more verification is needed. This may be the first estimate of the UHI effect derived from a global model while considering both UHI local heating and large-scale feedbacks. Previous data estimates of the global UHI, which considered the effect of urban areas but did not treat feedbacks or isolate temperature change due to urban surfaces from other causes of urban temperature change, imply a smaller UHI effect but of similar order. White roofs change surface albedo and affect energy demand. A worldwide conversion to white roofs, accounting for their albedo effect only, was calculated to cool population-weighted temperatures by ~0.02 K but to warm the earth overall by ~0.07 K. White roof local cooling may also affect energy use, thus emissions, a factor not accounted for here. As such, conclusions here regarding white roofs apply only to the assumptions made.

1. Introduction

Urban areas are generally warmer than vegetated areas around them since urban surfaces reduce evapotranspiration and have sufficiently different heat capacities, thermal conductivities, albedos, and emissivities to enhance urban warming (Howard 1833; Oke 1982). Several studies have estimated, from data analysis, that the globally averaged urban heat island (UHI) effect may contribute ≤0.1 K to global temperature changes since the preindustrial era (Jones et al. 1990; Easterling et al. 1997; Hansen et al. 1999; Peterson 2003; Parker 2006). The Intergovernmental Panel on Climate Change (IPCC) Fourth Assessment Report concluded that the UHI may have increased temperatures ~0.065 over land and ~0.022 K globally from 1900 to 2008 (Solomon et al. 2007, section 3.2.2.2). The IPCC global estimate was scaled from the land estimate assuming no UHI heating or feedbacks over the ocean. Data analysis studies of the UHI do not account for feedbacks of changes in local temperatures, moisture, and their gradients to large-scale weather systems, either due to traceable effects or to deterministic chaotic variation. Furthermore, such studies cannot distinguish temperature changes in urban areas due to the UHI from those due to greenhouse gases, carbon dioxide domes over cities (Jacobson 2010a), cooling or warming aerosol particles, transmission or use of electricity, stationary or mobile combustion, or human respiration, which also occur in urban areas. As such, numerical modeling is needed to isolate the UHI effect.

Whereas, several regional computer modeling studies of the UHI effect have been performed (e.g., Velazquez-Lozada et al. 2005; Sarrat et al. 2006), these studies did not provide information about feedbacks to the global scale. Recently, McCarthy et al. (2010) examined the global climate response of the addition of waste heat to urban areas but did not quantify the urban heat island effect due to such areas by removing urban land uses or examining climate responses outside of urban areas. Similarly, Oleson et al. (2011) added subgrid urban treatment to a global climate model and examined urban–rural temperature differences, which were determined with fixed sea surface temperatures and sea

Corresponding author address: M. Z. Jacobson, Department of Civil and Environmental Engineering, Stanford University, Stanford, CA 94305.
E-mail: jacobson@stanford.edu

DOI: 10.1175/JCLI-D-11-00032.1

ice. The study demonstrated strong warming in urban areas relative to surrounding rural areas due to the UHI but did not examine temperature changes beyond the urban regions. To our knowledge, no previous global study has quantified the global UHI effect, accounting for the climate responses of urban changes to the larger-scale sea surface temperatures, sea ice, atmospheric stability, aerosols, gases, clouds, and precipitation. This study aims to quantify the net effect of all urban areas on global climate with a model that resolves urban surfaces to their actual resolution and treats their feedbacks to the large scale while considering the statistical significance of results. The study does not examine the UHI contamination in global temperature measurements but rather the UHI contribution to actual global temperatures.

One geoengineering proposal to ameliorate the effects of the UHI contribution to global warming has been to use reflective roofing material or to paint existing roofs white. White roofs have generally been thought to reduce summer air conditioning energy demand and change the albedo of the surface. In such cases, the impact of converting roofs to white coatings should be to cool roofs initially (e.g., Sailor 1994; Simpson and McPherson 1997; Akbari et al. 2001). Akbari et al. (2009) estimated the surface albedo change from using reflective coatings on all roofs and pavements worldwide. That study used scaling arguments to estimate the equivalent carbon dioxide savings due to cooler global temperatures following such a conversion. However, they did not use a global model to simulate whether the conversion caused a net cooling or warming of global climate.

Menon et al. (2010) went further by using a land surface model to calculate the change in surface temperature due to changing all urban albedos worldwide by 0.1 and estimated a cooling. However, they did not calculate the climate response with an atmospheric model. As a result, they did not account for the effects of the albedo change on atmospheric stability, clouds, or the feedbacks to large-scale meteorology or climate. Oleson et al. (2010) expanded on these studies by treating white roofs in a global climate model as subgrid phenomena, also accounting for changes in air conditioning and space heating demand. Although their model included feedbacks to the larger scale, they reported temperature differences only between urban areas and nearby rural areas, so they did not determine the globally averaged temperature change due to white roofs. While they found a net cooling in urban areas due to white roofs as with the previous studies, they also found that white roofs increased space heating in the annual average more than they decreased air conditioning use (which occurs mostly in the summer).

Here, we use the same 3D model and input satellite data as we use to treat the UHI effect to estimate the climate response of theoretically converting all roofs within urban areas worldwide to white roofs. We report results globally and map the locations where results are found to be statistically significant.

2. Model description

The computer model used for this study was a one-way-nested (feeding information from coarser to finer domains) global-regional gas, aerosol, transport, radiation, general circulation, mesoscale, and ocean model (GATOR-GCMOM) that attempts to simulate climate, weather, and air pollution on all scales. For the present study, only the global domain was used (no nesting) but with treatment of subgrid surfaces.

The model and its algorithms have been compared with gas, aerosol, radiative, meteorological, and surface data and numerical solutions in over 50 studies. Surface solar irradiances in the presence of clouds were compared with hourly data paired in time and space, and other cloud parameters were compared with satellite data in Jacobson et al. (2007). In one comparison (Fig. 2 of that paper), the model was able to predict the observed presence or absence of low clouds on 25 of 28 days in February at a specific location. On four consecutive days, the model predicted the correct magnitude of solar reduction due to clouds. Modeled global precipitation fields, global lightning from satellite, surface ozone, and tropospheric–stratospheric ozone profiles were compared with data in Jacobson and Streets (2009). In this case, the model was able to simulate the observed peaks in global lightning flash rate by accounting for modeled bounceoffs following collision and charge separation of hydrometeor particles. Modeled vertical aerosol profiles, Arctic and Antarctic sea ice areas, and satellite fields of cloud fraction were evaluated against data in Jacobson (2010b). Satellite-derived fields of the relative humidity over ice at 200 hPa, contrail cloud fraction, and in situ vertical profiles of black carbon, temperature, and dewpoint were compared with the model in Jacobson et al. (2011). Whitt et al. (2011) compared zonally averaged static stability and tropopause height from satellite data with the model. The comparison of model results with vertical profile data in these studies suggests a lack of numerical diffusion with respect to vertical transport of gases and particles in the model. The model was also applied and evaluated with respect to subgrid land surface treatments and changes in Jacobson (2001a,b, 2008). The equilibrium sensitivity of the model to a doubling of CO_2 was found to be 3.2 K in Jacobson (2002).

The model simulates dynamical meteorology (pressures, geopotential heights temperatures, moisture, winds, turbulence); transport of gases and aerosols from the predicted winds and turbulent diffusivities; emissions and transformations of gases and aerosols; formation and evolution of size- and composition-resolved clouds from size- and composition-resolved aerosol particles; spectral radiative transfer through gases, aerosols, and clouds; ocean chemistry and transport; and subgrid surface processes. Gas processes include emissions, photochemistry, gas-to-particle conversion, gas-to-cloud conversion, gas–cloud exchange, gas–ocean exchange, advection, convection, molecular diffusion, turbulent diffusion, and dry deposition. Aerosol processes include anthropogenic and natural emissions, binary and ternary homogeneous nucleation, condensation, dissolution, internal-particle chemical equilibrium, aerosol–aerosol coagulation, aerosol–hydrometeor coagulation, sedimentation, dry deposition, and transport. Cloud microphysical processes include size- and composition-resolved liquid and ice activation and growth, coagulation, breakup, bounceoff, evaporative freezing, contact freezing, homogeneous freezing, heterogeneous freezing, sedimentation, subcloud evaporation–sublimation, and the tracking of all aerosol constituents through cloud drops, ice crystals, and graupel.

Here, the model treated two discrete aerosol size distributions, each with 14 size bins (2 nm to 50 mm in diameter), and three hydrometeor distributions (liquid, ice, and graupel), each with 30 size bins (0.5 to 8 mm in diameter). The two aerosol distributions included an emitted fossil-fuel soot (EFFS) and an internally-mixed (IM) distribution. EFFS emission sources included vehicles, power plants, industry, ships, and aircraft. IM emissions included sea spray, soil dust, ocean and soil bacteria, volcanic particles, pollen, spores, biofuel burning particles, and biomass-burning particles. Particle number and mole concentrations of several chemicals were predicted in each aerosol and hydrometeor size bin of each distribution. Table 1 of Jacobson (2010b) lists the chemical species included in each size distribution.

In each grid cell of the global domain, the model treated multiple subgrid cumulus clouds and grid-scale stratus clouds. Cloud thermodynamics was solved with equilibrium parameterizations. However, cloud microphysics was solved with time-dependent (nonequilibrium) numerical methods as a function of aerosol and hydrometeor particle size and composition (Jacobson 2003, 2010b; Jacobson et al. 2007).

The radiative transfer equation was solved numerically over each of 694 solar plus thermal–IR wavelengths–probability intervals in each cloudy and clear portion of each model column to obtain heating rates and actinic fluxes. Optical property treatments of gases, aerosol particles, and clouds are described in Jacobson (2010b).

The main strength of the model is the details and resolution of gas, aerosol, cloud, radiative, and surface processes. The main weakness is the significant computer time required, inhibiting global simulations longer than 20–25 years.

3. Subgrid surfaces

The model treated subgrid surface processes and energy and vapor exchange between the atmosphere and the subgrid surfaces. Seventeen subgrid surfaces classes were included in each grid cell, including 13 soil classes, water bodies, roads, roofs, and deep snow–ice (Table 1). The method of calculating the area of each grid cell covered with each surface class is discussed shortly. The treatments of subgrid surfaces and numerical methods used to solve energy and moisture fluxes through them are largely described in Jacobson (2001a), who developed subgrid urban surface treatments for all domains of a global-through-urban model.

Within each surface grid cell, subsurface soil temperatures and moisture (and their fluxes) were calculated over time in separate columns of each subgrid soil class with a 10-layer subsurface module (with top-to-bottom layer thicknesses of 0.005, 0.01, 0.01, 0.01, 0.015, 0.025, 0.05, 0.1, 5, and 5 m, respectively). Soil properties for each soil class are given in Jacobson (2005a, Table 6). Thus, subgrid, subsurface temperatures and moisture were tracked perpetually and independently throughout each model simulation. The same 10-layer subsurface module was applied to permanent snow (e.g., over the Antarctic) and to roads and rooftops.

Each subgrid soil class was divided into vegetated and bare soil. Snow could accumulate on both soil and vegetation. For bare and vegetated soil, the surface energy balance equation accounted for latent heat, sensible heat, solar, thermal–IR, and conductive energy fluxes. However, for vegetated soil, the fluxes took into account the foliage temperature and moisture as well as the temperature and moisture of the air within the foliage, all of which were tracked prognostically in time or diagnostically from prognostic parameters through a series of iterative calculations (Jacobson 2001a). Foliage temperature and moisture were a function of evapotranspiration, a process that conserves water in the model. The net surface flux over a subgrid soil class was an area-weighted average of the fluxes over vegetated and bare soil. When snow was present on top of vegetation or bare soil, an additional model layer with thickness equal to that of the snow was added to the 10-layer subsurface module.

TABLE 1. Fraction of the globe consisting of each surface type and the annually averaged vegetation fraction of the surface type. Data are shown both for cases when urban surfaces were included and excluded. The text describes the method of determining these values. Roads include other impervious ground material, including sidewalks and patios. Urban areas comprise 0.1283% of the global surface area in this dataset. Of the urban area, 52.157% is vegetated soil, 1.565% is bare soil, 27.767% is rooftop, and 18.511% is impervious material (roads). As such, 46.278% of the urban area or 0.05937% of the global surface area is road plus rooftop area. The area of the earth is $\sim 5.106 \times 10^8$ km^2.

	With urban surfaces		No urban surfaces	
	Surface fraction	Vegetation fraction	Surface fraction	Vegetation fraction
Sand	0.004 237	0.381 930	0.004 252	0.381 861
Loamy sand	0.011 238	0.530 809	0.011 271	0.530 404
Sandy loam	0.076 616	0.503 288	0.076 742	0.502 964
Silt loam	0.008 230	0.681 433	0.008 270	0.680 197
Silt	0.000 000 75	0.673 881	0.000 000 75	0.673 881
Loam	0.056 860	0.512 960	0.056 998	0.512 573
Sandy clay loam	0.042 356	0.564 198	0.042 433	0.563 828
Silty clay loam	0.000 814	0.681 287	0.000 818	0.680 017
Clay loam	0.018 789	0.717 948	0.018 865	0.716 327
Sandy clay	0.002 595	0.729 913	0.002 604	0.728 721
Silty clay	0.000 291	0.460 233	0.000 292	0.459 761
Clay	0.027 357	0.788 563	0.027 431	0.787 480
Peat	0.004 417	0.620 978	0.004 419	0.620 874
Water bodies	0.714 598	0	0.714 598	0
Deep snow/ice	0.031 006	0	0.031 006	0
Roads	0.000 237	0	0	0
Roofs	0.000 356	0	0	0
Total/average	1.000 000	0.145 205	1.000 000	0.145 413

Oceans in the model were represented in 3D for some calculations and 2D for others. A 2D time-dependent mixed layer ocean dynamics model driven by surface wind stress was used to solve for mixed layer velocities, heights, and horizontal energy transport in each grid cell (Ketefian and Jacobson 2009). The scheme conserves potential enstrophy, vorticity, energy, and mass and predicts gyres and major currents. Energy diffusion to the deep ocean was treated in 3D through 10 ocean layers below each surface grid cell. Air ocean exchange, vertical diffusion through the ocean, and 3D ocean equilibrium chemistry and pH were solved as in Jacobson (2005b).

Sea ice in the model could form on water surfaces, and snow could accumulate on sea ice. The model solved for the temperature at the ice–ocean interface, the snow–ice interface, the air–snow interface, and the air–ice interface as in Jacobson (2001a), which assumed single layers of sea ice and snow on top of sea ice whose thicknesses were solved for over time. When the weight of sea ice plus snow caused the sea ice to submerge below sea level, snow was converted to sea ice (e.g., Leppäranta 1983). Although snow on top of sea ice was treated as one layer, the density profile in the layer was calculated from (Herron and Langway 1980), and other properties of snow varied with density.

For permanent snow over land, the 10-layer subsurface model was used to transport energy through snow. Snow densities were calculated as a function of depth (Herron and Langway 1980) and other properties varied with density. For all snow, sea ice, and water surfaces, an additional layer was added to the bottom of the atmospheric radiative transfer calculation to solve for radiation fluxes through snow, ice, and water, respectively. The purpose of adding this layer was to predict, rather than prescribe, the albedo at the snow–air, ice–air, and water–air interface, particularly in the presence of pollutants such as black carbon, brown carbon, and soil dust (Jacobson 2004).

4. Treatment of urban surfaces

The fraction of each model grid cell consisting of each subsurface class was determined as follows. First, soil data at 10-km resolution for the world (Food and Agricultural Organization 1995) and at 1-km for the United States (Miller and White 1998) were used to determine the fraction of each soil class in each grid cell. The vegetation fraction inside each soil class was then determined each month from global vegetation fraction data derived from 2005 1-km Moderate Resolution Imaging Spectroradiometer (MODIS) *Terra* normalized difference vegetation index (NDVI) data (MOD13A3) (Huete et al. 2002; U.S. Geological Survey 2008) and an equation converting NDVI to vegetation fraction (see http://www.osdpd.noaa.gov/ml/land/gvi.html). The 1-km NDVI data were interpolated to 0.01° resolution for use in the model. Table 1 gives the fraction of the earth consisting of each soil class

TABLE 2. Annually averaged fraction of the globe consisting of each land cover type based on U.S. Geological Survey (2006) land use data interpolated to 0.01° × 0.01° resolution. The area of the earth is ~5.106 × 10^8 km^2.

Land cover type	Global fraction
Water bodies	0.715 186
Evergreen needleleaf forests	0.009 572
Evergreen broadleaf forests	0.025 970
Deciduous needleleaf forests	0.005 303
Deciduous broadleaf forests	0.004 162
Mixed forests	0.011 589
Closed shrubland	0.004 952
Open shrubland	0.038 964
Woody savannah	0.026 174
Savannah	0.016 864
Grassland	0.029 882
Permanent wetland	0.003 306
Cropland	0.023 770
Urban and built-up land	0.001 283
Cropland/natural veg. mosaic	0.016 527
Deep snow/ice	0.030 947
Barren or sparsely vegetated	0.035 550
Total	1.000 000

and the annually averaged vegetation fraction of each soil class based on these data. About 14.52% of the earth in 2005 was covered with vegetation (Table 1).

Next, world 2005 land use data, derived from the MODIS combined *Terra* and *Aqua* sensors (MCD12Q1) together with the International Geosphere-Biosphere Programme (IGBP) classification scheme, were interpolated from 500-m resolution to 0.01° resolution to correspond with the model resolution of the MODIS NDVI data (Loveland et al. 2000; U.S. Geological Survey 2006; Friedl et al. 2010). The land use data were then applied to determine the fraction of each model grid cell containing urban and built-up land, other land use surface types, and water bodies (Table 2). The MODIS NDVI data were subsequently used to determine the vegetation fraction (f_v) within each 0.01° × 0.01° urban pixel. The remainder of each urban pixel was divided into bare soil, impervious surfaces (termed roads), and rooftops. Bare soil was approximated as $f_s = 0.03 f_v$. The average ratio of roofs to roads for each 0.01° urban area was set to 1.5:1, close to the value from Jacobson (2001a), so the fractional roof area of an urban pixel was $f_{\text{roof}} = 0.6\,(1 - f_v - f_s)$ and the fraction of roads was $f_{\text{road}} = 0.4\,(1 - f_v - f_s)$. Based on this methodology, the smallest possible nonzero urban area or nonurban surface class in a grid cell was 1 km^2. However, since urban areas consisted of vegetated areas, roofs, plus roads, the smallest nonzero road plus roof area of a grid cell could be much less than 1 km^2.

According to these data, about 0.128% of the total earth or 0.504% of the world's nonpermanent ice-covered land (which represents 25.4% of the earth) was covered

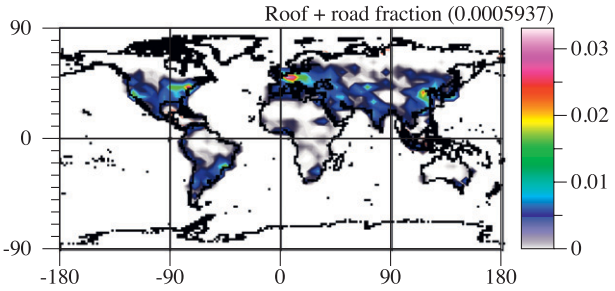

FIG. 1. Global distribution of road plus rooftop fraction worldwide in 2005 as determined by combining 0.01° land use data and 1-km vegetation fraction data. The global road plus roof fraction (0.000 594) is about 46.28% of the global 2005 urban land use fraction (0.001 28).

with urban surfaces in 2005 (Table 2). This urban surface area (~656 040 km^2) represents about 1.6 times the area of the state of California. For comparison, 1992 global land use data, derived from Advanced Very High Resolution Radiometer (AVHRR) data also using the IGBP classification scheme, indicate that ~0.0515% of the earth was covered with urban surfaces (U.S. Geological Survey 1999; Jacobson 2001a, Table 1). Thus, based on the comparison of satellite data products, the urban fraction of the earth may have increased by 249% in 13 years. The total urban area calculated here for 2005 (0.128% of total global area) is less than the 0.7% of global area estimated in Menon et al. (2010) from a coarse 0.5°-resolution dataset based on city lights. We believe the higher 0.01°-resolution dataset used here may be more representative of global urban land use area.

Of the total urban area in 2005, 52.2% was determined from the MODIS NDVI data to be vegetated soil, 1.57% was estimated to be bare soil, 27.8% was estimated to be rooftops, and 18.5% was estimated to be impervious surfaces. As such, 46.3% of urban pixels consisted of rooftops plus impervious surface material. Figure 1 shows the global distribution of roof plus road surfaces determined by this methodology. The global roof and road areas were 181 900 and 121 300 km^2, respectively. These areas compare with 380 000 and 530 000 km^2 assumed in Akbari et al. (2009) without the benefit of satellite analysis. They estimated that urban surface areas comprised 1% of all land (or 0.29% of the total earth), which is about 2.26 times greater than that estimated by the satellite analysis here. They also assumed a roof to road ratio of 0.71:1 versus 1.5:1 estimated here. Walls were ignored here for radiative calculations since radiative transfer and subsurface heat–moisture fluxes were calculated in columns.

As stated, roads and roofs were treated at their actual scale in the model since the model treated subgrid surfaces. When present, roads and roofs affected model

input parameters both at the surface and below the surface. Surface parameters in the model affected by urbanization included albedo, emissivity, vegetation fraction, leaf area index, and roughness lengths for momentum, heat, and moisture. Subsurface parameters affected included thermal conductivity, bulk density, specific heat, thermal diffusivity, and saturation moisture content. When roads and roofs were present, their vegetation fractions were zero (vegetation still comprised much of the rest of the urban surface area), but when roads and roofs were absent, the soil they replaced was assumed to be vegetated with the same vegetation fraction as the nonroad, nonroof areas in the urban area. Also, when roads and roofs were present, the soil moisture content of layers that included these materials was zero but the soil under roads contained moisture. When roads and roofs were removed, the combined road and roof area was replaced by the soil category that occupied the road or roof area, as determined from the soil and land use datasets combined, increasing the fractional soil coverage of each affected soil. The vegetation fraction of each soil class in each grid cell was also incremented. Table 1 compares the fraction of the earth consisting of each soil type and the fraction of vegetation in each soil category with and without urban surfaces, resulting from this methodology. When roofs were converted to white roofs, only the albedo of the roofs was changed, not the fractional soil or vegetation coverage.

For heat flux calculations here, roads and other impervious surfaces were assumed to consist of 5-cm-thick asphalt, impermeable to water and with asphalt properties (Anandakumar 1999), overlying soil. In terms of the 10-layer subsurface module that was applied to road surfaces, the top five layers were treated as asphalt, and the remaining layers were treated as a soil–air–water mixture, where the soil classification was determined from the soil dataset (Jacobson 2001a). Snow and liquid water could accumulate on the asphalt as an additional (11th) layer in the subsurface module.

Although roof types vary worldwide, asphalt shingles dominate in cities. The average rooftop was assumed to consist of 1.5-cm-thick asphalt shingles over 1 cm of asphalt–felt composite (saturated felt) over 1.25 cm of plywood over air (Jacobson 2001a). In terms of the 10-layer subsurface module, the top three layers consisted of each of these respective materials. Air (inside the building) composed the remaining seven layers (Jacobson 2001a). Asphalt shingles and asphalt–felt composites were assumed to have properties similar to asphalt. No liquid water passed through roofs but water and snow could deposit onto them as an additional layer.

During each subsurface module time step (15 s), surface and subsurface temperatures and moisture, sensible heat fluxes, latent heat fluxes, water vapor fluxes, friction wind speeds, Monin–Obhukov lengths, Richardson numbers, snow depths, ice thicknesses, sublimation rates, runoff, foliage temperatures, leaf stomata specific humidities, foliage air temperatures, foliage specific humidities, and water–snow stored on leaves, roads, and roofs were calculated for each surface class in each grid cell from the column subsurface module and stored (Jacobson 2001a). At the end of the time step, surface temperatures, sensible heat fluxes, latent heat fluxes, and water vapor fluxes were weighted by the fractional surface type in the cell to give an effective value for the whole cell. The weighting of fluxes calculated separately for each surface type is more physical than calculating a single-cell-averaged flux from averaged surface properties. Jacobson (2001a,b, Fig. 3 in both studies) compare modeled temperatures from this method with hourly data over four days at two dozen locations, including in cities.

The surface albedo of each grid cell at each wavelength was calculated as the area-weighted sum of the albedos of each surface class in the cell. For water, snow, and sea ice, spectral albedos were calculated prognostically by adding a water, snow, or sea ice layer below all atmospheric layers for each column radiative transfer calculation, which was performed online (Jacobson 2004). The albedos of roads and roofs were assumed to be those of asphalt. Solar albedos of paved asphalt range from 0.04 (new) to 0.17 (aged), averaging 0.12 (Pon 1999). Albedos for all other surfaces were obtained from 0.05°-resolution MODIS combined *Terra* plus *Aqua* satellite data in seven spectral bands (U.S. Geological Survey 2007; Schaaf et al. 2002). These solar albedos were interpolated spatially and spectrally to each of 86 solar wavelengths below 800 nm and 232 solar–IR wavelengths–probability intervals from 800 to 5000 nm. The model also solved thermal–IR radiative transfer over 376 thermal–IR wavelengths–probability intervals up to 1000 μm (Jacobson 2005c). For simulations analyzing the effects of white roofs, the solar albedos of all roofs were increased from 0.12 to 0.65, with no other changes. Since rooftops represented ~27.767% of urban surface area (Table 1), this represents an increase of ~0.147 in the overall urban albedo, slightly larger than the 0.10 increase assumed in Menon et al. (2010). The rooftop albedo change also represents only a 0.000 19 increase in the global surface albedo.

5. Urban heat island simulation results

Equilibrium climate simulations over a global domain were first run with and without urban surfaces (roads and roofs), for 20 years. This case is referred to as the

UHI1 case. An additional simulation with all roofs converted to white roofs was then run. In addition, six random-perturbation simulations were run for three years to test the statistical significance of results from the three main simulations during the same period. Finally, results from the UHI1 case are compared with those from an earlier simulation pair (UHI2) run with fewer vertical layers to evaluate the robustness of results.

The horizontal grid-scale model resolution in all cases was 4°SN × 5°WE, but subgrid surfaces were treated as described earlier. All simulations except the UHI2 simulations included 58 sigma-pressure vertical layers up to 0.219 hPa (≈60 km), with 37 layers up to 12 km and 15 layers below 1 km. The UHI2 simulations included 47 vertical layers up to 0.219 hPa, including 6 layers in the bottom 1 km. In all cases, the model was initialized with 1° × 1° reanalysis meteorological fields (Global Forecast System 2010) for simulations starting 1 January 2006 and run forward in time with no data assimilation or model spinup.

The global- and simulation-averaged road, roof, and top-soil temperatures in the base case were 293.14, 290.61, and 286.25 K, respectively (Table 3), indicating that road and roof temperatures were 3–7 K higher than soil temperatures, in range of measurements (Oke 1982; Anandakumar 1999; Bornstein and Lin 2000). The higher road versus roof temperature was expected (Jacobson 2001a). The surface air temperature differences over land between the simulations with and without urban surfaces (UHI1 case) were +0.31 K when temperature changes were weighted by population, +0.22 K averaged over all land, and +0.11 globally (Fig. 2a, Table 3). Significant model drift occurred during the first decade of simulation. However, the globally averaged temperature change due to the UHI in the model after 12 years was similar to that after 20 years, suggesting minimal model drift during the last 8 years of simulation. For the UHI2 case, the warming was +0.16 K when weighted by population, +0.11 K over land, and +0.062 K globally. Some of the differences between the UHI1 and UHI2 cases are due to the difference in model setup (e.g., different number of layers) and some are due to the deterministic chaotic variation, discussed shortly.

The temperature changes above are contributions to gross global warming, not net warming. Gross global warming is the warming due to all factors that increase global temperatures over time. Net warming is gross warming minus factors that decrease global temperatures. Net global warming from all causes between 1850–99 and 2001–05 has been estimated to be about +0.76 ±0.19 K (Solomon et al. 2007). This net change is primarily due to warming from greenhouse gases (2–2.4 K) plus fossil-fuel and biofuel soot aerosol particles (0.4–0.7 K) (Jacobson 2010b) and the global UHI effect (+0.06 to +0.11 K here from the UHI1 and UHI2 simulations) offset by cooling due to nonsoot aerosol particles (−1.7 to −2.3 K) and albedo–evapotranspiration change due to deforestation (0 to −0.4 K). Thus, the UHI may represent about 2%–4% of gross global warming based on these two sets of simulations. However, because these ranges reflect differences in model results from two sets of simulations, and results from all models vary with improvements in resolution and new data, the range of uncertainty is likely larger than the range of results provided here.

The UHI temperature increase calculated for the world here of 0.06–0.11 K, which accounts for feedbacks to the large scale and isolates the urban surface contribution to warming from all other causes of urban warming–cooling, is ~2.7–5 times higher than UHI temperature increase estimate of 0.022 K globally for 1900–2008 based on data analysis (Solomon et al. 2007, section 3.2.2.2). The IPCC estimate, however, does not account for feedbacks and does not isolate the urban surface contribution to urban warming from all causes of urban warming. More specifically, it accounts only for temperature differences between urban versus rural areas, and temperature changes in urban areas are due to multiple factors aside from changes in urban surfaces. For example, urban temperature changes are also due to greenhouse gases, carbon dioxide domes over cities, black and brown carbon, cooling aerosol particles, heat released due the transmission and use of electricity, heat released during stationary and mobile combustion, and human respiration. Thus, the IPCC reports a net temperature difference due to all causes of urban temperature change, a large portion of which is cooling due to aerosol particle pollution, rather than a temperature difference that isolates the effects of urban surfaces on warming, as calculated here. Further, the data analysis estimate does not account for feedbacks of the UHI to the large scale (e.g., over the ocean and poles). In fact, the IPCC report states explicitly that effects over the ocean are assumed to be zero. Despite these differences, the proximity of the model results to the data analysis results suggests that the UHI appears to be a relative small component of gross global warming (2%–4%).

To check the statistical significance of the sensitivity test pairs relative to natural variations in the climate system/model arising from the fact that atmospheric dynamical processes are deterministically chaotic (Lorenz 1963), six random perturbation simulations in which the initial value of one parameter was varied at one location on the global domain were run for three years. Three years was justified because significance test results for three years were similar to those for one and two years for

TABLE 3. Globally- and simulation-averaged baseline simulation results, percent differences between baseline and no-urban-surface simulation results (in the UHI1 case), and percent differences between the white roofs and baseline simulation results. Population-weighted results and differences are also shown. Population-weighted values are changes in each grid cell multiplied by its population, summed over all cells, and divided by the world population. Parameters indicating ''land'' or ''ocean'' are averages over land and ocean, respectively. Divide mg m^{-2} by 1.9637 to obtain the global burden in Tg. Note the following abbreviations: aerosol optical depth (AOD). Single-scattering albedo (SSA), cloud optical depth (COD), turbulent kinetic energy (TKE), relative humidity (RH), and particulate matter (PM). Albedo from land cover is the albedo derived from satellite data used to initialize the radiative transfer calculation. The albedo from radiative transfer is the albedo calculated from the radiative transfer code, accounting for a layer of ocean water, lake water, sea ice, or snow if they are present and for the current composition of the atmosphere and angle of the sun.

Parameters	Baseline world	Base − no urban surface (% change world)	White roofs − base (% change)	Pop-weighted baseline world	Pop-weighted base − no urban surfaces (% change world)	Pop-weighted white roofs − base (% change)
45-m air temperature (K)	288.48	+0.0385	+0.022	295.08	+0.093	−0.0065
15-m air temperature (K)	288.17	+0.0397	+0.024	294.85	+0.104	−0.0072
Global ground temp (K)	288.85	+0.0373	+0.025	295.23	+0.0927	−0.0143
Air T 45 m − air T 15 m (K)	+0.31	−0.0012	−0.002	+0.23	−0.011	+0.0007
Air T 15m − ground T (K)	−0.68	+0.0024	−0.001	−0.38	+0.0113	+0.0071
Land air temp (K)	282.78	+0.0796	+0.0722			
Land ground temp (K)	282.62	+0.0776	+0.0027			
Day surface air temp (K)	289.55	+0.0363	+0.0214			
Night surface air temp (K)	287.99	+0.0382	+0.0253			
Day ground temp (K)	290.22	+0.0355	+0.0224			
Night ground temp (K)	287.40	+0.0393	+0.0278			
Soil temp (K)	286.25	+0.0675	+0.0094			
Ocean temp (K)	293.63	+0.0109	+0.0085			
Latent heat (J m^2 s^{-1}, + up)	73.1	−0.019	+0.165	65.6	−0.016	−0.13
Sensible heat (J m^2 s^{-1}, + up)	15.1	−0.012	−0.255	33.0	+1.22	−0.20
45-m wind speed (m s^{-1})	6.43	−0.154	+0.020	4.75	−0.41	+0.294
15-m wind speed (m s^{-1})	5.48	−0.070	+0.085	3.71	+0.22	+0.14
TKE (m^2 s^{-2})	0.267	−0.203	−0.014	0.394	+0.018	+0.17
650-nm COD	12.5	−0.154	−0.301	14.8	−0.53	−0.78
Cloud liquid (kg m^{-2})	0.138	+0.195	+0.138	0.152	−0.050	−0.96
Cloud ice (kg m^{-2})	0.0571	+0.102	−0.0945	0.0685	−0.32	−1.0
Cloud fraction	0.635	−0.168	+0.114	0.550	−0.77	−0.63
Precipitation (mm day^{-1})	2.69	−0.0151	+0.173	2.66	−0.41	−0.86
Surface thermal–IR (W m^{-2})	−61.6	+0.256	+0.064	−75.8	+1.05	+0.40
Surface solar (W m^{-2})	159	+0.136	+0.113	170	+0.38	+0.14
Near-surface RH (fraction)	0.733	−0.096	+0.0041	0.590	−1.07	−0.26
Soil moist (m^3 m^{-3}) (land)	0.246	−0.844	−0.0158	0.171	−1.55	−0.04
Sea ice depth (m)	0.153	+4.0	−1.39	$6.9x10^{-5}$	−6.7	−6.3
Snow depth (m)	4.69	−0.56	−0.611	0.0154	−10.6	−0.14
Albedo from land cover	0.184	−0.933	−0.478	0.121	−0.30	+1.3
Albedo from rad. transfer	0.145	−0.876	−1.23	0.115	−2.03	+0.73
Surface O_3 (ppbv)	15.4	+0.154	+1.06	23.2	+1.1	+0.081
Surface Peroxyacetyl nitrate (PAN) (ppbv)	0.582	−0.165	−0.803	1.62	+0.052	−0.17
Surface CO (ppbv)	251	+0.397	+0.112	334	−0.66	+0.033
Surface formaldehyde (HCHO) (ppbv)	1.23	+1.03	+0.147	3.53	+1.4	−0.15
Surface toluene (ppbv)	0.086	−1.55	−0.166	0.548	−2.9	−0.14
Surface isoprene (ppbv)	1.04	+1.22	−0.157	2.37	+1.0	−0.47
Surface SO_2 (ppbv)	0.321	−1.1	+0.116	3.45	−3.4	+0.66
Surface $PM_{2.5}$ (mg m^{-3})	24.4	−0.649	−0.828	39.0	−3.6	−1.0
Surface dry $PM_{2.5}$ (mg m^{-3})	10.3	−0.172	−2.12	30.7	−0.99	−1.4
Surface soil dust (mg m^{-3})	6.03	−0.368	−5.77	17.3	−0.37	−4.2
550-nm AOD	0.132	−0.571	−1.16	0.198	−0.73	−0.67
550-nm surface SSA	0.936	−0.021	−0.0029	0.758	−0.17	−0.034

the present study and similar to results for three or four years for related studies conducted.

Near-surface air temperature differences from the simulations with and without urban surfaces were then compared with the standard deviation among the random-perturbation simulations within each model surface grid cell with a nondirectional t test in a manner similar to in Chervin and Schneider (1976). The resulting confidence

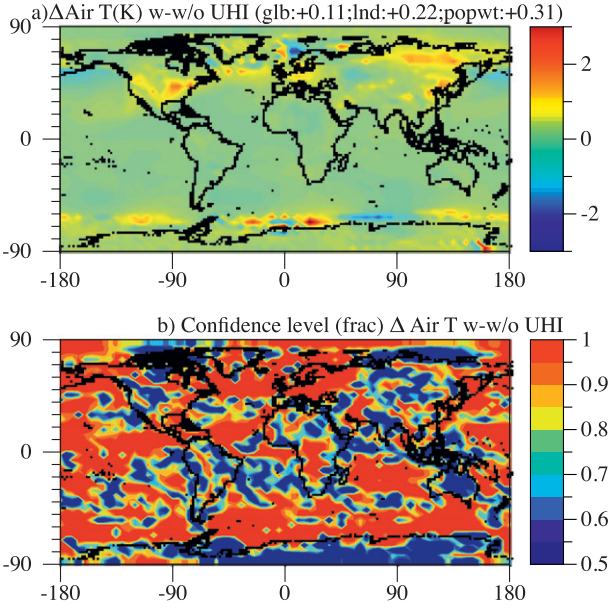

FIG. 2. (a) The simulated UHI effect and its feedbacks to the larger scale, averaged over 20 years. (b) Corresponding plots of the confidence level of the results from a nondirectional *t* test relative to six random-perturbation simulations accounting for deterministic chaotic variation (internal variability) over the first three years of simulation.

levels (CLs) in each model grid cell of the statistical significance of the spatial temperature changes are shown in Fig. 2b. CLs of 95% or higher suggest strong statistical significance. Results for about 43% of the earth were significant to the 95% CL; results for 33% of the earth were significant to the 98% CL. Less significant results occurred mostly in the Southern Hemisphere, particularly where temperature changes were small, although some occurred in the U.S. Great Plains and over the Sahara. Differences for the baseline minus no-urban-surfaces case were also statistically significant to a 95% CL over 15%–65% of the earth for all other globally averaged parameters in Table 3.

Another method of analyzing the statistical significance of results is to examine the spatial correlation between the fraction of urban surfaces and the resulting temperature change in the grid cell with that fraction. Figure 3 shows such a correlation plot as well as a plot showing the correlation between a random fraction in the grid cell and ground temperature in the same cell from the same simulation. Figure 3a indicates that ground temperature changes from the 20-yr baseline simulation increased with increasing urban fraction and that the correlation was strongly statistically significant ($p < 0.0001$). The r value decreased somewhat (from $r = 0.36$ to $r = 0.20$) but p remained <0.0001 when the highest 10% urban fraction areas were removed, suggesting that the largest urban areas dominated the correlation.

Ground temperature changes were not correlated spatially with a random variable ($p = 0.86$) (Fig. 3b), suggesting again that the UHI heating for urban cities was not an artifact of model deterministic chaotic variation at those locations. Table 3 and Fig. 2a indicate that the population-weighted air temperature change owing to the UHI was about 2.6 times the globally averaged air temperature change owing to the UHI, again indicating that the modeled UHI impact on global temperatures was dominated by temperature changes in population centers.

The modeled globally averaged vertical air temperature change (Fig. 4) because of the UHI effect indicates that the UHI effect is primarily a near-surface phenomenon, although some warming did extend up to 200 hPa. It does not explain much of observed upper-tropospheric warming since 1958 (Randel et al. 2009) (Fig. 4a). Upper-tropospheric warming can be explained better by greenhouse gases and soot particles (e.g., Solomon et al. 2007; Jacobson 2010b).

The causes of the modeled temperature increases are studied more in depth here by analyzing feedbacks among atmospheric variables in the UHI1 case. The surface heating due to the UHI increased the upward sensible heat flux over populated areas but decreased such fluxes in the global average (Table 3, Fig. 5a). The sensible heat flux depends primarily on surface wind shear and buoyancy. Table 3 indicates that the UHI enhanced instability between 15 and 45 m much more in the population-weighted average than in the global average. Table 3 also indicates that the resulting turbulence mixed fast winds from 45 m down to 15 m, decreasing wind speeds at 45 m and increasing them at 15 m in the population-weighted average. The wind speed increase at 15 m increased wind shear, which along with warmer surface temperatures, increased turbulent kinetic energy (TKE) as shown in Table 3, increasing the sensible heat flux from the surface. TKE increases occurred significantly in the eastern United States, Europe, and eastern China, locations of heavy urbanization (Fig. 1), but not in the global average.

The UHI slightly decreased the upward latent heat flux averaged over all urban areas and in the global average, although it increased the upward latent heat flux over much of Europe and the northeast United States (Table 3, Fig. 5b). The net reduction in latent heat flux in urban areas may be expected since impervious surfaces reduce the transfer of moisture from the soil to the atmosphere. The reduced evaporation contributes to the warmer ground and surface air, increasing the upward sensible heat flux. However, since urban areas and their

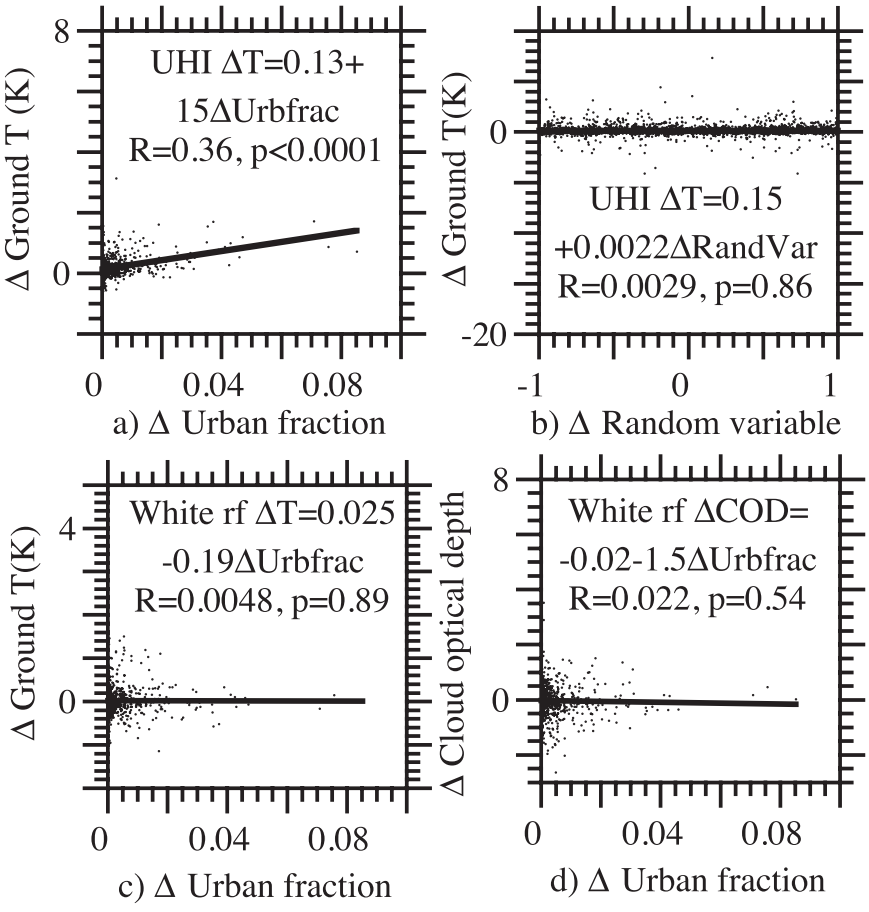

FIG. 3. Correlation plots between 20-yr-modeled (a) urban fraction and ground temperature change due to the UHI effect, (b) a random value for urban fraction and ground temperature change due to the UHI effect, (c) urban fraction and ground temperature change due to white roofs, and (d) urban fraction and cloud optical depth changes due to white roofs. Each plot is from the same simulation; each pair of values in each plot is from a different surface grid cell.

surroundings still contained exposed soil, higher temperatures there enhanced evaporation from such soil, increasing latent heat fluxes in some areas.

Higher temperatures in urban areas caused a population-weighted 1% reduction in the near-surface relative humidity (Table 3, Fig. 5c). The reduced relative humidity reduced population-weighted cloud optical depth, liquid, ice, and fraction (Table 3, Fig. 5d), increasing surface solar radiation (Table 3, Fig. 5e) and surface heating in a positive feedback. The increase in surface solar occurred over both urban and nonurban regions where cloud optical depths decreased (Figs. 5d,e). However, the enhanced upward sensible heat flux due to the UHI enhanced convection sufficiently over North America, Eastern Europe, and much of Southeast Asia to enhance precipitation in those regions (Figs. 5a,f). The UHI reduced precipitation in western Europe slightly, which coincided with a decrease in cloud optical depth there (Fig. 5d).

The increase in precipitation near most urbanized areas in the United States and China, for example, in Fig. 5f is consistent with regional studies that found increases in precipitation in or downwind of urban areas, generally due to enhanced convection from heating or changes in roughness due to urbanization (e.g., Changnon 1981; Jauregui and Romales 1996; Bornstein and Lin 2000; Niyogi et al. 2006; Hand and Shepherd 2009; Shem and Shepherd 2009). The overall reduction in precipitation worldwide was due to reductions primarily in the tropics caused by meteorological feedbacks to pressures, winds, and cloudiness there. Precipitation is greater in magnitude in the tropics than at other latitudes; therefore, smaller relative precipitation reductions in the tropics resulted in larger-magnitude reductions

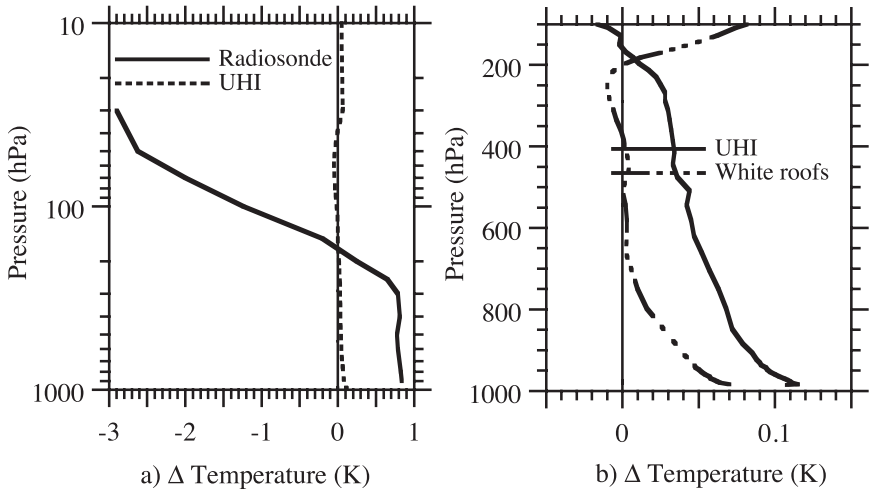

FIG. 4. Globally averaged vertical profile difference in the air temperature due to the simulation-averaged modeled (a) UHI effect and (b) the UHI effect and white roofs, separately. Also shown in (a) is the globally averaged vertical profile of radiosonde-derived temperatures in 2007 minus those in 1958 (Randel et al. 2009).

there than increases at other latitudes, causing a net precipitation reduction worldwide.

An additional feedback to discuss is that to ozone. Higher temperatures in and around urban areas should increase ozone when ozone is already high since higher temperatures thermally dissociate more organic nitrate compounds to organic gases and nitrogen oxides, both precursors to ozone, and such compounds are more abundant where ozone is high (Jacobson 2010a). In addition, higher temperatures cause more emissions of biogenic organics, such as isoprene, from vegetation. Third, increases in ultraviolet sunlight also increase ozone. Table 3 indicates that the UHI increased temperatures, solar (thus UV) radiation, isoprene, and ozone. Figure 5g shows that substantial ozone increases occurred in and around urban areas identified in Fig. 1. The increase in urban ozone due to the UHI effect was a result similar to the increase in ozone due to CO_2 domes forming over cities (Jacobson 2010a). In both cases, the ozone increases were triggered by higher temperatures. However, the UHI effect decreased latent heat fluxes, resulting in less population-weighted cloudiness immediately over urban areas (as opposed to downwind), more UV flux to the surface, and more ozone. CO_2 domes, on the other hand, increased evaporation and higher water vapor enhances chemical ozone production as well (Jacobson 2010a).

The UHI decreased near-surface particle concentrations in the population-weighted average, partly by increasing vertical dilution of particles by increasing TKE in urban areas (Table 3) and partly by increasing precipitation over polluted urban regions (the major removal mechanism of particles). Figure 5h indicates that dry $PM_{2.5}$ (particulate matter smaller than 2.5 μm in diameter) decreases occurred substantially in locations of precipitation increases (Fig. 5f), namely the eastern United States and eastern China. Decreases also occurred in Europe and parts of northwestern Africa, where upward sensible heat fluxes and thus vertical turbulence were strong (Fig. 5a). Dry $PM_{2.5}$ increases occurred in western Asia and were attributable mostly to increases in soil dust because of increases in wind speeds. Worldwide, the reduction in dry $PM_{2.5}$ was slightly less than the reduction in world soil dust suggesting that changes to the nonsoil-dust dry $PM_{2.5}$ worldwide were near zero (Table 3). However, population-weighted soil dust decreases were less than population-weighted nonsoil-dust dry $PM_{2.5}$ decreases, suggesting precipitation and sensible heat changes played a more dominant role in urban areas. The urban $PM_{2.5}$ decrease due to the UHI differs from the urban $PM_{2.5}$ increase due to CO_2 domes since CO_2 domes stabilize the air, reducing vertical dilution (Jacobson 2010a), whereas the UHI destabilizes the air, increasing vertical dilution.

6. Similarities and differences between UHI and other causes of warming

The UHI effect differs from greenhouse gases and absorbing particle effects in terms of both the height at which warming occurs (e.g., Fig. 4) and the mechanisms of warming. Whereas, greenhouse gases absorb thermal–IR radiation and absorbing aerosol particles absorb solar radiation, the UHI both reduces evapotranspiration (reducing water vapor transfer to the air, reducing

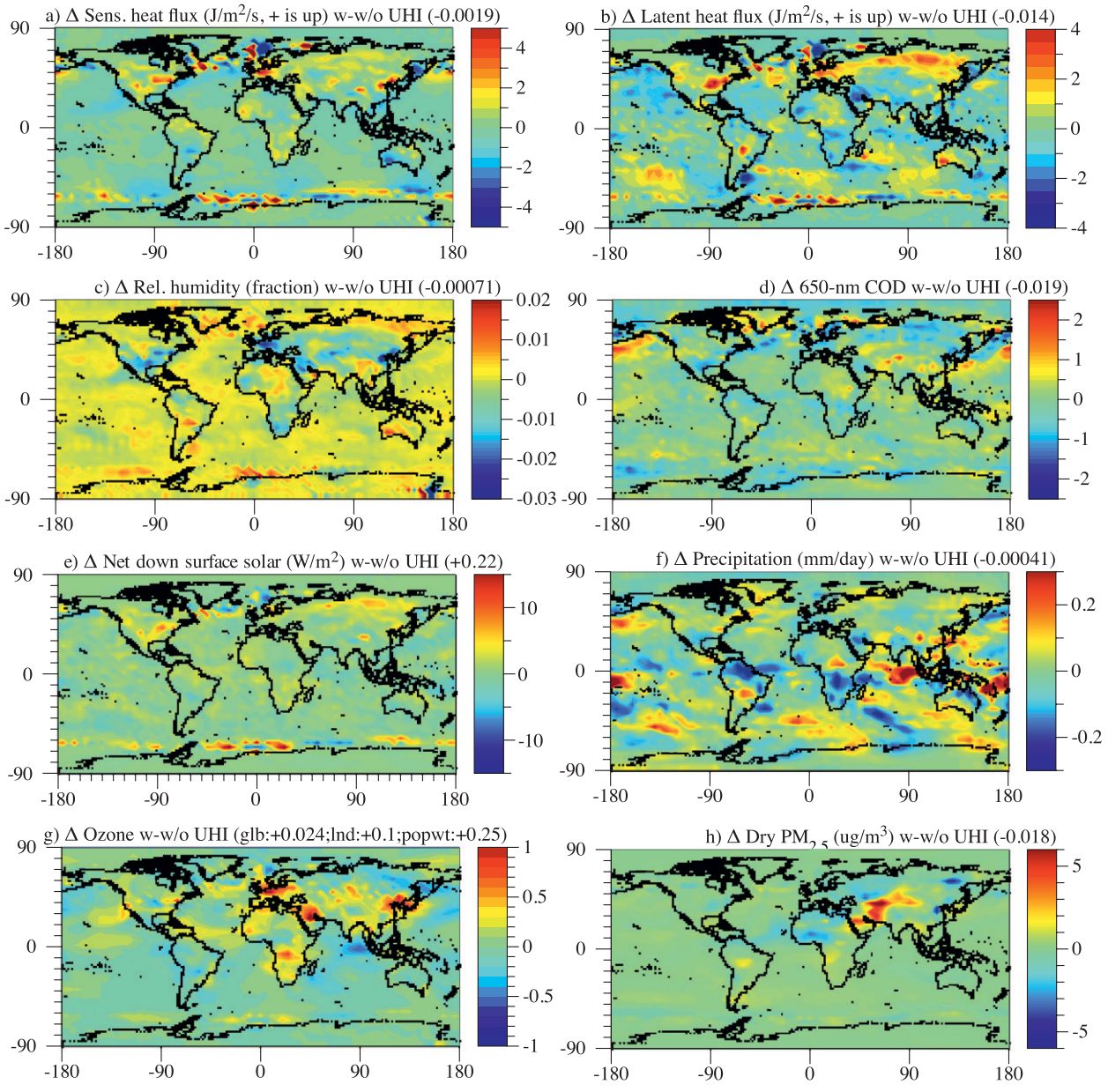

FIG. 5. The 20-yr simulation-averaged global difference in the several variables (one in each panel) due to the UHI effect.

evaporative cooling) and warms material surfaces directly during the day. Temperature increases due to the direct warming of material surfaces are dampened by the increase in thermal–IR emissions that accompanies the surface warming. However, the permanent reduction in evapotranspiration, the higher equilibrium temperature of the urban surface, and the resulting changes in sensible, latent, and radiative energy fluxes add a permanent forcing to the climate system.

Urban areas can affect a larger percent of the world than they occupy in a manner somewhat similar to how absorbing aerosol particles and greenhouse gases affect a larger percent of the world than they are emitted from. Short- and long-lived pollutants emitted from urban regions feedback locally to clouds but also mix hemispherically within a week, affecting meteorology on the large scale. Similarly, energy and moisture changes from urban areas affect local cloud formation but also mix hemispherically within a week, as energy and moisture are transferred by the same winds as are pollutants. Since urban areas are distributed throughout the world (Fig. 1), global changes in energy and moisture due to urban areas may be observed in less than a week.

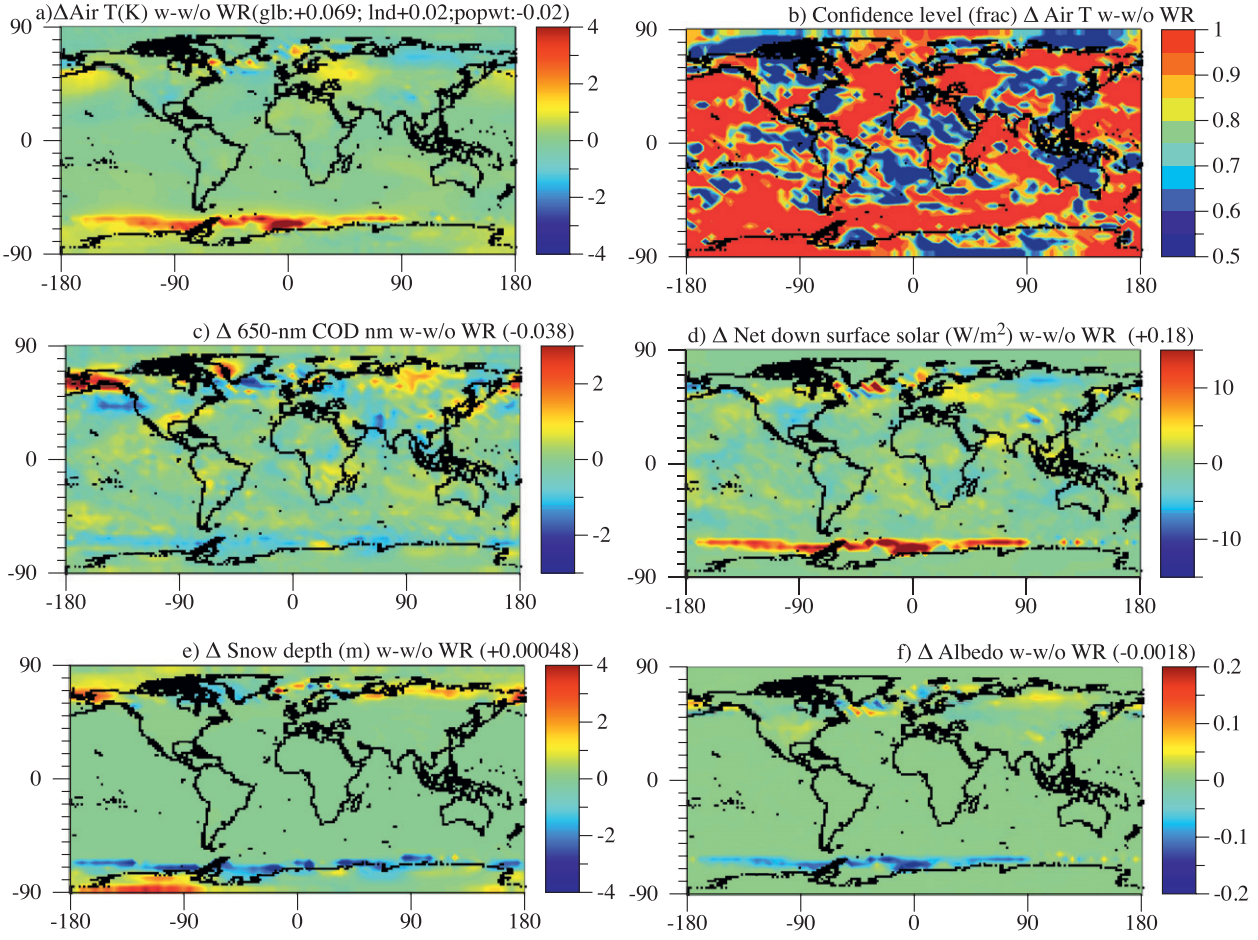

FIG. 6. (a) A 20-yr simulation-averaged perturbations in surface temperature due to the inclusion of white roofs (WRs). (b) Corresponding plots of the confidence level of the results from a nondirectional *t* test relative to six random-perturbation simulations over the first three years of simulation. (c)–(f) Modeled global difference in the several variables (one in each panel) due to white roofs from the same simulations.

Further, urban heat islands can trigger temperature changes in nearby areas in a positive feedback. For example, warm air from an urban area that advects to a snowy rural area can help to melt the snow and reduce surface albedo in a positive feedback. Such feedbacks cannot be captured with data analysis or with simulations that compare temperature differences between urban and rural areas. They can be captured with simulations that include then exclude urban areas since heat and moisture fluxes depend on the properties of the surface materials present or not present.

7. White roof simulation results

An additional 20-yr simulation was run in which all roofs worldwide were converted to white roofs by increasing the solar albedos of the original roofs from 0.12 to 0.65 (section 3), with no other change. White coatings have been hypothesized to cool roofs locally (Sailor 1994; Simpson and McPherson 1997; Akbari et al. 2001), and this hypothesis was confirmed in the model results. Table 3 and Fig. 6a show that conversion to white roofs cooled population-weighted ground and air temperatures over the simulation. However, feedbacks of the local changes to the large scale resulted in a gross global warming but smaller in magnitude than the UHI. Whereas, the population-weighted air temperature decrease due to white roofs was ~0.02 K, the global temperature increase was ~0.07 K (Fig. 6a). A second simulation (not shown) using 1992 land use data resulted in a similar conclusion: local cooling but global warming due to white roofs.

Figure 6b suggests that the near-surface temperature change results over three years were statistically significant to a 95% CL compared with six random-perturbation simulations over about 43% of the earth and to a 98% CL

over 32% of the earth. In addition, differences for the white roofs minus baseline case were statistically significant to a 95% CL over 15%–55% of the earth for all other globally-averaged parameters in Table 3. Thus, the white roof results, while statistically significant over much of the earth, were slightly less significant than the UHI results.

Figure 3c shows a negative spatial correlation between an increasing urban fraction and ground temperature change (thus cooler local ground temperatures with increasing urban fraction) in the white roofs case. However, the results of this test were not statistically significant. The reason for the modest negative correlation appears to be that local cooling of roofs owing to the increase in population-weighted surface albedo resulting from their enhanced reflectivity (Table 3) decreased population-weighted upward sensible and latent heat fluxes (Table 3), in turn reducing population-weighted cloud fraction and cloud liquid and ice optical depths (Table 3), thus increasing population-weighted surface solar radiation (Table 3), offsetting much of the benefit of the local cooling due to the local albedo increase.

The decrease in sensible heat flux was due to the fact that white roofs stabilized air near the ground in urban areas, as evidenced by the greater decrease in population-weighted ground temperature than 15-m air temperature and the greater decrease in 15-m air temperature than 45-m air temperature due to white roofs in Table 3. Population-weighted TKE increased in this case because of the increase in surface wind speed (Table 3), most likely resulting from the greater pressure gradients between rural and urban areas caused by the local cooling from white roofs. Wind shear affects air primarily in the surface layer, whereas sensible heat fluxes affect air further above the surface layer, so the reduced sensible heat flux caused most of the enhanced stability and cloud reduction due to white roofs. Whereas, white roofs stabilized air locally, they destabilized air globally (Fig. 4b) because of the surface warming caused by white roofs away from urban areas.

Figure 3d illustrates that white roofs decreased cloud optical depths more in grid columns with high urban surface fractions than with low urban fractions, although the correlation was not statistically significant. A comparison of Fig. 6c with Fig. 1 also indicates that decreases in cloud optical depth occurred substantially over areas with high urban fractions. Although roofs are a small fraction of the earth, they are distributed (Fig. 1) so white roofs caused small changes in clouds, pressures, and winds in many locations simultaneously. Such changes fed back to temperatures, pressures, and winds, altering cloudiness in other locations. Cloud changes over high latitudes had some of the greatest impacts. Cloud increases over northern latitudes (Fig. 6c) increased precipitation and decreased surface solar radiation there (Fig. 6d), increasing snow depth (Fig. 6e) and thus surface albedo (Fig. 6f), decreasing temperatures (Fig. 6a) in a positive feedback. Since the albedo of new snow is substantially higher than that of sea ice or land, the addition of snow to sea ice or land increases the local albedo as does the addition of sea ice to the ocean surface.

Conversely, cloud decreases at the edge of Southern Hemisphere sea ice (Fig. 6c) increased surface solar radiation (Fig. 6d), decreasing snow cover (Fig. 6e), decreasing albedo (Fig. 6f), and increasing temperatures there (Fig. 6a) in a positive feedback. Figure 6f indicates that changes in surface albedo due to changes in snow, ice, and atmospheric composition far from urban areas in other parts of the world can exceed in magnitude the original change in albedo due to the white roofs. It is well known that the climate over high latitudes is more sensitive to changes than over low latitudes because of strong feedbacks to snow and sea ice albedo.

Another impact of decreasing the surface albedo by increasing white roofs is to increase the solar absorption by black carbon and UV–visible-absorbing brown carbon in soot particles. With greater surface reflection, soot can absorb not only downward solar radiation but also upward solar. The model treated such absorption. Table 3 indicates that white roofs slightly decreased the population-weighted near-surface single-scattering albedo (SSA) and the global near-surface SSA to a lesser extent, suggesting an increase in atmospheric heating due to the enhanced reflection. While soot has a short lifetime, the air heated by the soot can travel long distances, suggesting an additional method by which local changes due to white roofs can propagate to the large scale.

In addition to affecting albedo, white roofs change energy use, thus greenhouse gas and warming and cooling pollutant aerosol particle emissions. Emissions decrease if white roofs cause summer cooling or increase if they cause winter warming. This feedback was not accounted but should be considered in any final assessment of the effects examined here. However, Oleson et al. (2010) found that, in the annual average, white roofs increased winter space heating more than they decreased summer air conditioning. If correct, this result suggests that the additional treatment of home energy use due to white roofs in the present case would only strengthen the conclusion found here that white roofs may contribute to local cooling but may or may not reduce global warming.

In sum, white roofs may increase or reduce local energy demand and reduce local temperatures. However, their local ground cooling stabilizes the surface air, reducing vertical sensible and latent heat fluxes, reducing

local cloudiness, and increasing local surface solar radiation, which in turn offsets some of their local cooling benefits. Higher reflection also increases local atmospheric heating by black and brown carbon in soot particles; however, the resulting feedback to temperature is minimal. Feedbacks of local changes to the global scale cause feedbacks magnified at high latitudes over snow and sea ice, causing a net effect on globally averaged temperatures that may be warming but is still highly uncertain. Thus, white roofs may reduce temperatures locally but may or may not reduce overall global warming.

8. Conclusions

This paper described results from two sets of 20-yr global simulations under different model conditions to examine (i) the effects of urban surfaces (roofs and impervious ground surfaces, termed roads) and (ii) converting roofs to white roofs on global climate. Roads and roofs were treated at their actual scale in the model. The model also treated multiple subgrid surface types in each surface grid cell. For heat island calculations, changes in urban surfaces affected the albedo, emissivity, vegetation fraction, leaf area index, and roughness lengths for momentum, heat, and moisture of the surface. They also affected the thermal conductivity, bulk density, specific heat, thermal diffusivity, and saturation moisture content of the subsurface. Conversion to white roofs affected only the albedo of the surface.

Global soil-type, vegetation fraction, albedo, and land use data were combined at high resolution to determine the contemporary characteristics of global land cover and urban surface area. The data suggest that, in 2005, ~0.128% of the earth was covered with an urban land use category, an increase over ~0.0515% in 1992. Data also suggest that about half of urban land cover is vegetated, on average, suggesting much of the rest is covered with impervious ground material (termed roads) and roofs.

Roads and roofs were modeled with 20-yr equilibrium climate simulations to have increased gross global warming (warming before cooling due to aerosol particles and albedo change from deforestation is accounted for) by 0.6–0.11 K (equally between day and night) and the population-weighted gross global temperature by 0.16–0.31 K. As such, the urban heat island (UHI) effect may contribute to 2%–4% of gross global warming. Because these ranges reflect differences in model results from two sets of simulations, and results from all models vary with improvements in resolution and new data, the range of uncertainty may be larger than the range of results provided here. Nevertheless, this appears to be the first estimate of the UHI effect derived from a global model and considers both local heating and feedbacks to the large scale. Previous estimates of the global-scale UHI from data analysis, which considered the effect of urban areas on local temperature change only and did not isolate the contribution of urban surface from other causes of urban temperature change, imply a smaller effect but of similar order.

The major feedback of the UHI to the large scale appears to be the increase in energy and decrease in moisture flux from urban areas to the large scale. Locally and on the large scale these changes decreased the relative humidity and cloudiness, increasing surface solar radiation in a positive feedback. Greater local convection increased precipitation downwind of many urban areas. The magnitude of the feedbacks depends on model resolution and treatments; thus, further work is needed to corroborate these results.

White roofs reduce summer air conditioning energy demand and change surface albedo. A conversion of rooftops worldwide to white roofs, accounting for their albedo effect only, was calculated to cool population-weighted global temperatures by ~0.02 K but to warm the earth overall by ~0.07 K. Local ground cooling stabilized surface air, reducing sensible and latent heat fluxes and local cloudiness, increasing local surface solar radiation, resulting in local cooling smaller in magnitude than without the cloud reduction. Higher reflection also increased air heating by black and brown carbon in soot. Feedbacks of local changes to the global scale were magnified over high-latitude snow and sea ice, causing a net but highly uncertain warming effect on global climate. The local cooling due to white roofs may reduce or increase energy demand and thus other emissions as well, a factor not accounted for in these simulations. This feedback should be considered in any final assessment of the effects of white roofs on climate.

Acknowledgments. This work was supported by NASA under Grant NNX07AN25G and the U.S. EPA under Grant RD-83337101-O. John Ten Hoeve also received support under a NASA Earth Systems Science Fellowship and a Stanford Graduate Fellowship.

REFERENCES

Akbari, H., M. Pomerantz, and H. Taha, 2001: Cool surfaces and shade trees to reduce energy use and improve air quality in urban areas. *Sol. Energy,* **70,** 295–310.

——, S. Menon, and A. Rosenfeld, 2009: Global cooling: Increasing world-wide urban albedos to offset CO_2. *Climatic Change,* **94** (3–4), 275–286, doi:10.1007/s10584-008-9515-9.

Anandakumar, K., 1999: A study of the partition of net radiation into heat fluxes on a dry asphalt surface. *Atmos. Environ.,* **33,** 3911–3918.

Bornstein, R. D., and Q. Lin, 2000: Urban heat islands and summertime convective thunderstorms in Atlanta: Three case studies. *Atmos. Environ.,* **34,** 507–516.

Changnon, S. A., Jr., Ed., 1981: METROMEX: A review and summary. *Meteor. Monogr.,* No. 40, Amer. Meteor. Soc., 181 pp.

Chervin, R. M., and S. H. Schneider, 1976: On determining the statistical significance of climate experiments with general circulation models. *J. Atmos. Sci.,* **33,** 405–412.

Easterling, D. R., and Coauthors, 1997: Maximum and minimum temperature trends for the globe. *Science,* **277,** 364–367.

Food and Agricultural Organization, 1995: Soil map of the world and derived soil properties (version 3.5). FAO Land and Water Digital Media Series 1, FAO, Rome Italy.

Friedl, M. A., D. Sulla-Menashe, B. Tan, A. Schneider, N. Ramankutty, A. Sibley, and X. Huang, 2010: MODIS Collection 5 global land cover: Algorithm refinements and characterization of new datasets. *Remote Sens. Environ.,* **114,** 168–182.

Global Forecast System, cited 2010: 1° × 1° reanalysis fields. [Available online at http://nomads.ncdc.noaa.gov/data/gfs-avn-hi/.]

Hand, L. M., and J. M. Shepherd, 2009: An investigation of warm-season spatial rainfall variability in Oklahoma City: Possible linkages to urbanization and prevailing wind. *J. Appl. Meteor. Climatol.,* **48,** 251–269.

Hansen, J., R. Ruedy, J. Glascoe, and M. Sato, 1999: GISS analysis of surface temperature change. *J. Geophys. Res.,* **104,** 30 997–31 022.

Herron, M. M., and C. C. Langway, 1980: Firn densification: An empirical model. *J. Glaciol.,* **25,** 373–385.

Howard, L., 1833: *The Climate of London*. Vols. I–III.

Huete, A., K. Didan, T. Miura, E. P. Rodriguez, X. Gao, and L. G. Ferreira, 2002: Overview of the radiometric and biophysical performance of the MODIS vegetation indices. *Remote Sens. Environ.,* **83,** 195–213.

Jacobson, M. Z., 2001a: GATOR-GCMM: A global through urban scale air pollution and weather forecast model. 1. Model design and treatment of subgrid soil, vegetation, roads, rooftops, water, sea ice, and snow. *J. Geophys. Res.,* **106,** 5385–5402.

——, 2001b: GATOR-GCMM: 2. A study of day- and nighttime ozone layers aloft, ozone in national parks, and weather during the SARMAP Field Campaign. *J. Geophys. Res.,* **106,** 5403–5420.

——, 2002: Control of fossil-fuel particulate black carbon plus organic matter, possibly the most effective method of slowing global warming. *J. Geophys. Res.,* **107,** 4410, doi:10.1029/2001JD001376.

——, 2003: Development of mixed-phase clouds from multiple aerosol size distributions and the effect of the clouds on aerosol removal. *J. Geophys. Res.,* **108,** 4245, doi:10.1029/2002JD002691.

——, 2004: Climate response of fossil fuel and biofuel soot, accounting for soot's feedback to snow and sea ice albedo and emissivity. *J. Geophys. Res.,* **109,** D21201, doi:10.1029/2004JD004945.

——, 2005a: *Fundamentals of Atmospheric Modeling*. 2nd ed Cambridge University Press, 813 pp.

——, 2005b: Studying ocean acidification with conservative, stable numerical schemes for nonequilibrium air-ocean exchange and ocean equilibrium chemistry. *J. Geophys. Res.,* **110,** D07302, doi:10.1029/2004JD005220.

——, 2005c: A refined method of parameterizing absorption coefficients among multiple gases simultaneously from line-by-line data. *J. Atmos. Sci.,* **62,** 506–517.

——, 2008: The short-term effects of agriculture on air pollution and climate in California. *J. Geophys. Res.,* **113,** D23101, doi:10.1029/2008JD010689.

——, 2010a: The enhancement of local air pollution by urban CO_2 domes. *Environ. Sci. Technol.,* **44,** 2497–2502, doi:10.1021/es903018m.

——, 2010b: Short-term effects of controlling fossil-fuel soot, biofuel soot and gases, and methane on climate, Arctic ice, and air pollution health. *J. Geophys. Res.,* **115,** D14209, doi:10.1029/2009JD013795.

——, and D. G. Streets, 2009: The influence of future anthropogenic emissions on climate, natural emissions, and air quality. *J. Geophys. Res.,* **114,** D08118, doi:10.1029/2008JD011476.

——, Y. J. Kaufman, and Y. Rudich, 2007: Examining feedbacks of aerosols to urban climate with a model that treats 3D clouds with aerosol inclusions. *J. Geophys. Res.,* **112,** D24205, doi:10.1029/2007JD008922.

——, J. T. Wilkerson, A. D. Naiman, and S. K. Lele, 2011: Effects of aircraft on climate and pollution. Part I: Numerical methods for treating the subgrid evolution of discrete size- and composition-resolved contrails from all commercial flights worldwide. *J. Comput. Phys.,* **230,** 5115–5132.

Jauregui, E., and E. Romales, 1996: Urban effects on convective precipitation in Mexico City. *Atmos. Environ.,* **30,** 3383–3389.

Jones, P. D., P. Ya. Groisman, M. Coughlan, N. Plummer, W. C. Wang, and T. R. Karl, 1990: Assessment of urbanization effects in time series of surface air temperature over land. *Nature,* **347,** 169–172.

Ketefian, G. S., and M. Z. Jacobson, 2009: A mass, energy, vorticity, and potential enstrophy conserving boundary treatment scheme for the shallow water equations. *J. Comput. Phys.,* **228,** 1–32, doi:10.1016/j.jcp.2008.08.009.

Leppäranta, M., 1983: A growth model for black ice, snow ice and snow thickness in subarctic basins. *Nord. Hydrol.,* **14,** 59–70.

Lorenz, E. N., 1963: Deterministic nonperiodic flows. *J. Atmos. Sci.,* **20,** 130–141.

Loveland, T. R., B. C. Reed, J. F. Brown, D. O. Ohlen, J. Zhu, L. Yang, and J. W. Merchant, 2000: Development of a global land cover characteristics database and IGBP DISCover from 1-km AVHRR Data. *Int. J. Remote Sens.,* **21,** 1303–1330.

McCarthy, M. P., M. J. Best, and R. A. Betts, 2010: Climate change in cities due to global warming and urban effects. *Geophys. Res. Lett.,* **37,** L09705, doi:10.1029/2010GL042845.

Menon, S., H. Akbari, S. Mahanama, I. Sednev, and R. Levinson, 2010: Radiative forcing and temperature response to changes in urban albedos and associated offsets. *Environ. Res. Lett.,* **5,** 014005, doi:10.1088/1748-9326/5/1/014005.

Miller, D. A., and White, R. A., 1998: A conterminous United States multi-layer soil characteristics data set for regional climate and hydrology modeling. *Earth Interact.,* **2**. [Available online at http://EarthInteractions.org.]

Niyogi, D., T. Holt, S. Zhong, P. C. Pyle, and J. Basara, 2006: Urban and land surface effects on the 30 July 2003 mesoscale convective system event observed in the southern Great Plains. *J. Geophys. Res.,* **111,** D19107, doi:10.1029/2005JD006746.

Oke, T. R., 1982: The energetic basis of the urban heat island. *Quart. J. Roy. Meteor. Soc.,* **108,** 1–24.

Oleson, K. W., G. B. Bonan, and J. Feddema, 2010: The effects of white roofs on urban temperature in a global climate model. *Geophys. Res. Lett.,* **37,** L03701, doi:10.1029/2009GL042194.

——, ——, ——, and T. Jackson, 2011: An examination of urban heat island characteristics in a global climate model. *Int. J. Climatol.,* **31,** 1848–1865, doi:10.1002/joc.2201.

Parker, D. E., 2006: A demonstration that large-scale warming is not urban. *J. Climate,* **19,** 2882–2895.

Peterson, T. C., 2003: Assessment of urban versus rural in situ surface temperatures in the contiguous United States: No difference found. *J. Climate,* **16,** 2941–2959.

Pon, B., cited 1999: Pavement albedo. Heat Island Group. [Available online at http://heatisland.lbl.gov/Pavements/Albedo/.]

Randel, W. J., and Coauthors, 2009: An update of observed stratospheric temperature trends. *J. Geophys. Res.,* **114,** D02107, doi:10.1029/2008JD010421.

Sailor, D. J., 1994: Simulated urban climate response to modifications in surface albedo and vegetative cover. *J. Appl. Meteor.,* **34,** 1694–1704.

Sarrat, C., A. Lemonsu, V. Masson, and D. Guedalla, 2006: Impact of urban heat island on regional atmospheric pollution. *Atmos. Environ.,* **40,** 1743–1758.

Schaaf, C., and Coauthors, 2002: First operational BRDF, albedo nadir reflectance products from MODIS. *Remote Sens. Environ.,* **83,** 135–148.

Shem, W., and M. Shepherd, 2009: On the impact of urbanization on summertime thunderstorms in Atlanta: Two numerical model case studies. *Atmos. Res.,* **92,** 172–189.

Simpson, J. R., and E. G. McPherson, 1997: The effects of roof albedo modification on cooling loads of scale model residences in Tucson. Arizona. *Energy Build.,* **25,** 127–137.

Solomon, S., D. Qin, M. Manning, M. Marquis, K. Averyt, M. M. B. Tignor, H. L. Miller Jr., and Z. Chen, Eds., 2007: *Climate Change 2007: The Physical Science Basis.* Cambridge University Press, 996 pp.

U.S. Geological Survey, 1999: 1-km resolution global land cover characteristics data base, derived from Advanced Very High Resolution Radiometer (AVHRR) data from the period April 1992 to March 1993.

——, cited 2006: Land cover type yearly L3 global 500 m V5 data, processed to 0.01°. [Available online at https://lpdaac.usgs.gov/lpdaac/products/modis_products_table/land_cover/yearly_l3_global_500_m/mcd12q1.]

——, cited 2007: *Terra* plus *Aqua* combined albedo 16-day L3 global 0.05° CMG V4 data. [Available online at https://lpdaac.usgs.gov/lpdaac/products/modis_products_table/brdf_albedo_model_parameters/16_day_l3_0_05deg_cmg/mcd43c1.]

——, cited 2008: Vegetation indices monthly L3 global 1 km V5 data, processed to 0.01°. Land Processes Distributed Active Archive Center. [Available online at https://lpdaac.usgs.gov/lpdaac/products/modis_products_table/vegetation_indices/monthly_l3_global_1km/mod13a3.]

Velazquez-Lozada, A., J. E. Gonzalez, and A. Winter, 2005: Urban heat island effect analysis for San Juan, Puerto Rico. *Atmos. Environ.,* **40,** 1731–1741.

Whitt, D. B., M. Z. Jacobson, J. T. Wilkerson, A. D. Naiman, and S. K. Lele, 2011: Vertical mixing of commercial aviation emissions from cruise altitude to the surface. *J. Geophys. Res.,* **116,** D14109, doi:10.1029/2010JD015532.